

**Ultrafast modification of the polarity at LaAlO<sub>3</sub>/SrTiO<sub>3</sub> interfaces**A. Rubano,<sup>1,5</sup> T. Günter,<sup>2</sup> M. Fiebig,<sup>2,3</sup> F. Mileto Granozio,<sup>1,4</sup> L. Marrucci,<sup>1,5</sup> and D. Paparo<sup>5,\*</sup><sup>1</sup>*Dipartimento di Fisica, Università di Napoli “Federico II,” Complesso Universitario di Monte S. Angelo, via Cintia, 80126 Napoli, Italy*<sup>2</sup>*Helmholtz-Institut für Strahlen- und Kernphysik, Universität Bonn, Nussallee 14-16, 53115 Bonn, Germany*<sup>3</sup>*Department of Materials, ETH Zürich, Vladimir-Prelog-Weg 4, 8093 Zurich, Switzerland*<sup>4</sup>*CNR-SPIN, Complesso Universitario di Monte S. Angelo, via Cintia, 80126 Napoli, Italy*<sup>5</sup>*Institute of Applied Science and Intelligent Systems, Via Campi Flegrei 34, 80078 Pozzuoli*

(Received 20 December 2016; revised manuscript received 4 January 2018; published 25 January 2018)

Oxide growth with semiconductorlike accuracy has led to atomically precise thin films and interfaces that exhibit a plethora of phases and functionalities not found in the oxide bulk material. This has yielded spectacular discoveries such as the conducting, magnetic, and even superconducting LaAlO<sub>3</sub>/SrTiO<sub>3</sub> interfaces separating two prototypical insulating perovskite materials. All these investigations, however, consider the static state at the interface, although studies on fast oxide interface dynamics would introduce a powerful degree of freedom to understanding the nature of the LaAlO<sub>3</sub>/SrTiO<sub>3</sub> interface state. Here, we show that the polarization state at the LaAlO<sub>3</sub>/SrTiO<sub>3</sub> interface can be optically enhanced or attenuated within picoseconds. Our observations are explained by a model based on charge propagation effects in the interfacial vicinity and transient polarization buildup at the interface.

DOI: [10.1103/PhysRevB.97.035438](https://doi.org/10.1103/PhysRevB.97.035438)**I. INTRODUCTION**

Interfaces between transition-metal oxides exhibit unique functionalities [1]. One of the most fascinating examples was the discovery of a high-mobility two-dimensional electron gas (2DEG) at the interface between two insulating perovskites, LaAlO<sub>3</sub> and SrTiO<sub>3</sub> (LAO/STO). [2] The 2DEG formation is a threshold process: For  $n \geq 4$  monolayers of LAO on STO the interface becomes metallic [3] and even superconducting [4]. At  $n = 3$  an electric field [3] or light [5] controls the phase at the LAO/STO interface so that a *reversible* insulator-to-metal transition (IMT) can occur. This may serve as the basis of optoelectronics applications [6,7], but with optical control on the time scale of seconds or longer.

In contrast, studies on fast oxide interface dynamics are still rare, although such investigations would be invaluable to understanding the nature of the LAO/STO interface state: Time dependence allows one to separate and recognize the various interactions contributing to the interfacial ground state via the different inherent time scales on which they respond after optical excitation. For example, transient ultrafast absorption spectroscopy led to evidence for the strong influence of the LAO film on self-trapped polaron formation at the LAO/STO interface [8].

Here, we reveal the mechanisms guiding buildup and depletion of photoinduced polarity at the LAO/STO interface. We obtain an optically induced subpicosecond *enhancement* or *attenuation* of interface polarity; both may exceed 50%. This effect is established by three competing photocarrier mechanisms: screening, asymmetric drift, and trapping. We track the LAO/STO carrier dynamics by all-optical time-resolved pump-probe spectroscopy, using second-harmonic

generation (SHG) as the probe process which detects the interfacial inhomogeneity while masking the bulk.

Optical SHG, i.e., doubling the frequency of a light wave, has emerged as a powerful tool for investigating oxide thin films, heterostructures, and interfaces [9–13]. Within the electric dipole approximation SHG is symmetry forbidden in the bulk of centrosymmetric materials. SHG is therefore ideal for probing interfaces and surfaces, where this violation occurs inherently [14].

Previous static SHG experiments provided valuable insight into the LAO/STO system [9,12,13,15–19]. We probed the behavior of the STO at the LAO/STO and air/STO interfaces with SHG photon energies up to 4 eV. After verifying that there are no contributions from the STO bulk, the LAO, or the LAO/air interfaces [9,12], we identified two components of the SHG susceptibility, denominated in the following as  $\chi_{\text{loc}}$  and  $\chi_{\text{ext}}$ , that completely describe the SHG spectroscopic features observed at the LAO/STO and STO/air interfaces [9,17]. Comparison of SHG from  $\chi_{\text{loc}}$  and  $\chi_{\text{ext}}$  allowed us to disentangle the particular role of the interfacial Ti<sup>4+</sup>(3d) orbitals [9,17,20].

In Sec. II we provide the details of the macroscopic model used to describe the SHG experimental data. In Sec. III we describe how samples are fabricated and our pump-probe SHG apparatus. In Sec. IV we present the experimental results obtained with both pump-probe reflectivity and pump-probe SHG measurements. Section V is devoted to discussing our results within the framework of a phenomenological model. Finally, we present our conclusions.

**II. SHG THEORY FOR SURFACES AND INTERFACES**

In SHG an optical wave with frequency  $2\omega$  is generated from an incident wave of frequency  $\omega$ . The actual measured

\*d.paparo@isasi.cnr.it

quantity is the SHG intensity  $I_{\text{SHG}}$ , which is proportional to the square of the reflected SHG optical field:  $I_{\text{SHG}} \propto |E_{\text{SHG}}(2\omega)|^2$ . The latter is, in turn, proportional to the square of the amplitude of the incident optical field,  $E_{\text{SHG}}(2\omega) \propto \chi E^2(\omega)$ , where  $\chi$  is, in general, defined as follows [18]:

$$\chi(t) = \int e_i^{2\omega} L_{ii}^{\text{out}} [\chi_{ijk}^{(2)}(z) + \chi_{ijkz}^{(3)}(z) E_z^{\text{pol}}(t, z)] \times L_{jj}^{\text{in}} L_{kk}^{\text{in}} e_j^\omega e_k^\omega dz, \quad (1)$$

where the sum on repeated indices is understood,  $z$  is the coordinate along the interface normal, and  $e^{2\omega, \omega}$  are the electric-field unit vectors in vacuum. In Eq. (1),  $\chi_{ijk}^{(2)}$  describes the structural symmetry breaking occurring at any interface, and  $\chi_{ijkl}^{(3)}$  with  $l = z$  parameterizes the coupling to the electric field  $E_z^{\text{pol}}$  that is generated by the space-charge region at the LAO/STO or STO/air interface [17]. In the latter case a space-charge region may be created by charged surface defects. An optical excitation will drive the space-charge distribution out of equilibrium, causing  $E_z^{\text{pol}}$  to become time dependent. In general,  $\chi_{ijk}^{(2)}$  and  $\chi_{ijkz}^{(3)}$  might also be time dependent because of the transient redistribution of the electronic populations by the pump beam, also known as the state-filling effect [21]. However, our measurements of photoinduced reflectivity, as discussed in Sec. IV B, indicate that these effects are negligible if compared to the free-carrier effects accounted for by  $E_z^{\text{pol}}$ ; hence, we will consider them to be a constant.  $\mathbf{L}$  is a diagonal tensor giving the Fresnel transformation matrices that parametrize the propagation between the different media. The complete expression for the three nonzero components of this tensor can be found in Ref. [20]. These factors may vary in time because of changes in the refractive index. However, based on the photoinduced reflectivity measurements, we can assume that the Fresnel factors vary too little to explain the absolute SHG signal variations or, in any case, they vary approximately in the same way for all the samples to account for the different dynamics observed among the samples. For all these reasons we neglect the Fresnel factors in our analysis.

In Eq. (1) the  $z$  integral extends across the entire thickness of the polar layer where inversion symmetry is broken by the presence of the interface [9] or by the photoinduced charge redistribution. We underline here that, unlike the standard optical techniques, the probing depth of SHG is not *a priori* fixed but depends on the spatial extension of the polar asymmetry at the specific interface under study. Since we measure the temporal, but not the spatial, dependence of the LAO/STO interface dynamics, we execute the  $z$  integration in Eq. (1) and resort to space-averaged susceptibilities:

$$\overleftrightarrow{\chi} = \chi_{ijk}(t) = \bar{\chi}_{ijk} + \Delta \bar{\chi}_{ijk}(t), \quad (2)$$

where  $\bar{\chi}_{ijk} = \int \chi_{ijk}^{(2)} dz + V_0 \chi_{ijkz}^{(3)}$  and  $\Delta \bar{\chi}_{ijk}(t) = \Delta V(t) \chi_{ijkz}^{(3)}$ . Note that  $\Delta \bar{\chi}_{ijk}(t)$  is the pump-induced variation of  $\bar{\chi}_{ijk}$ ; thus, it is null for  $t < 0$ . Here, we have introduced the ground-state energy depth  $V_0$  of the quantum well induced by  $E_z^{\text{pol}}(z, t < 0)$  at the LAO/STO (STO/air) interface and its light-induced variation  $\Delta V(t)$ . By using suitable polarization combinations of the light all the elements of the  $\overleftrightarrow{\chi}$  tensor can be measured.

As detailed in Ref. [20], only three SHG contributions need to be distinguished for probing the LAO/STO interface:  $\chi_{zzz}$ ,

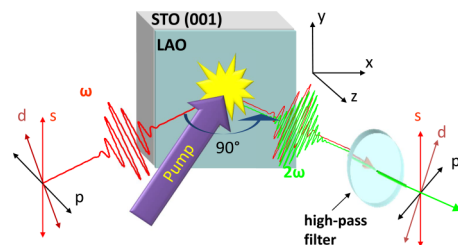


FIG. 1. SHG pump-probe layout and geometry of the input/output light polarizations. The high-pass filter blocks the fundamental beam. The latter is removed during the photoinduced reflectivity measurements.

$\chi_{zzz}$ , and  $\chi_{xxz}$ . The susceptibility  $\chi_{xxz}$  (and thus  $\bar{\chi}_{xxz}$ ,  $\Delta \bar{\chi}_{xxz}$ ) couples to the transition from the  $O^{2-}$  ( $2p$ )-dominated STO valence band to the lowest STO conduction subbands, mainly formed by the  $Ti^{4+}$  ( $3d_{xy}$ ) orbitals. In complement,  $\chi_{zxx}$  (and thus  $\bar{\chi}_{zxx}$ ,  $\Delta \bar{\chi}_{zxx}$ ) represents the transition to the  $Ti^{4+}$  ( $3d_{xz, yz}$ ) orbitals. The third component,  $\chi_{zzz}$ , is not considered here since it cannot be measured directly and couples to the same transition as  $\chi_{xxz}$  anyway. Note that the subbands with a  $d_{xy}$  character are more localized at the interface [22–24], whereas those with a  $d_{xz, yz}$  character are more extended, so that  $\chi_{xxz}$  and thus  $\Delta \bar{\chi}_{xxz}$  (henceforth  $\chi_{\text{loc}}$  and  $\Delta \bar{\chi}_{\text{loc}}$ ) and  $\chi_{zxx}$  and thus  $\Delta \bar{\chi}_{zxx}$  (henceforth  $\chi_{\text{ext}}$  and  $\Delta \bar{\chi}_{\text{ext}}$ ) predominantly probe the local state at the interface and the extended environment around it, respectively. We stress here that that “extended” (ext) and “localized” (loc) states differ only for few atomic layers; that is, both must be considered interfacial states that cannot be probed by standard optical techniques.

### III. EXPERIMENT

#### A. Sample fabrication

LAO films of two and six unit cells were deposited by pulsed-laser deposition on  $TiO_2$ -terminated STO(001) substrates with unit-cell control of the film thickness by high-energy electron diffraction. The samples were grown at  $\approx 800^\circ\text{C}$  in  $1 \times 10^{-4}$  mbar oxygen atmosphere and then cooled at this pressure to room temperature. All samples with a LAO thickness above the threshold of four unit cells show the same qualitative dynamics. Therefore, in this work, we focus our attention on two representative samples with a LAO film of two (LS2) or six (LS6) unit cells. LS2 and LS6 represent the LAO/STO samples with initially insulating and initially conducting interfaces, respectively, exhibiting sheet conductance at 300 K of  $< 10^{-9} \Omega^{-1}$  (LS2) and  $\approx 10^{-4} \Omega^{-1}$  (LS6). Our pump beam excites photocarriers at 4.35 eV, i.e., above the direct band gap of  $SrTiO_3$  of about 3.75 eV [25], but not across the bulk band of LAO, so most of the observed dynamics resides in STO. We therefore include the air/STO interface dynamics of a  $TiO_2$ -terminated STO(001) substrate in our investigation.

#### B. SHG and reflectivity pump-probe experiments

The pump-probe layout is shown in Fig. 1. As a light source we used two phase-locked optical parametric amplifiers pumped by a single amplified Ti:sapphire laser system (130-fs

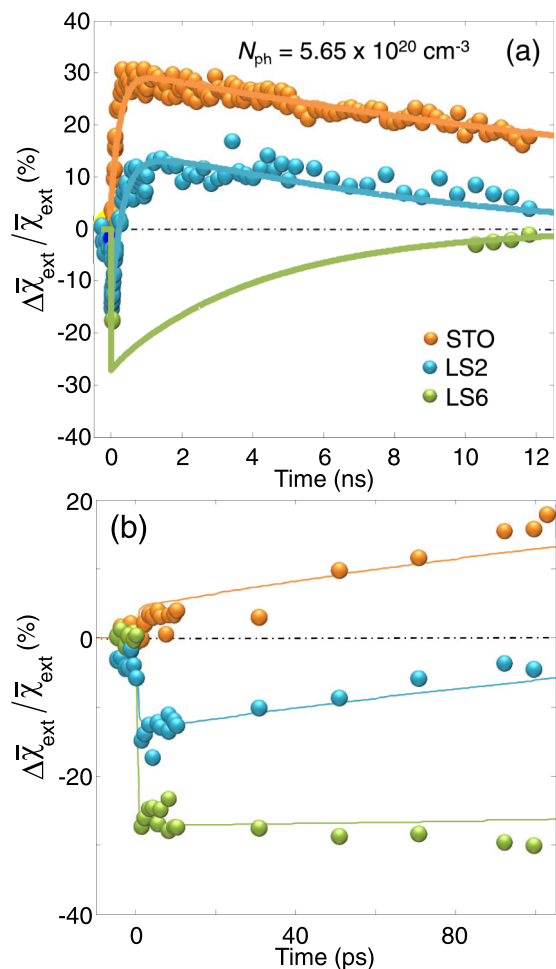


FIG. 2. (a) and (b) Temporal evolution of  $\Delta\bar{\chi}_{\text{ext}}/\bar{\chi}_{\text{ext}}$  for  $N_{\text{ph}} = 5.65 \times 10^{20} \text{ cm}^{-3}$ . Solid lines are fits (see text for details). Note the striking difference of the dynamics between insulating (orange and blue points) and conductive (green points) samples that points to a complex interplay of different photoinduced mechanisms better explained in the text.

pulse duration, 1-kHz repetition rate, 1.55 eV nm central photon energy). The absorption length of the pump beam at a photon energy of 4.35 eV is 26 nm [26].

The pump beam was focused onto an area of  $280 \pm 14 \mu\text{m}$ . Because of the very small pump-pulse energy of 0.1 nJ to 2  $\mu\text{J}$ , sample heating and deterioration are negligible. To probe the lowest cross-band-gap electronic states of the STO, the probe beam was tuned to an SHG photon energy of 3.75 eV. In order to subtract any long-term background the pump beam is chopped at 500 Hz, and the difference in the SHG signal of two consecutive probe pulses is measured. This allows an accurate determination of the ultrafast response, while any dynamics exceeding 1 ms cannot be recorded. The data points shown in Figs. 2 and 3 are given by the difference in the square roots of the two consecutive probe intensities normalized to the square root of the SHG intensity at time  $t < 0$ .

In Fig. 1 the geometry of the input/output light polarizations is shown. According to the fourfold rotational symmetry ( $4mm$ ) of the interface, we measured the only three independent nonvanishing polarization combinations:  $p$  in,  $p$  out

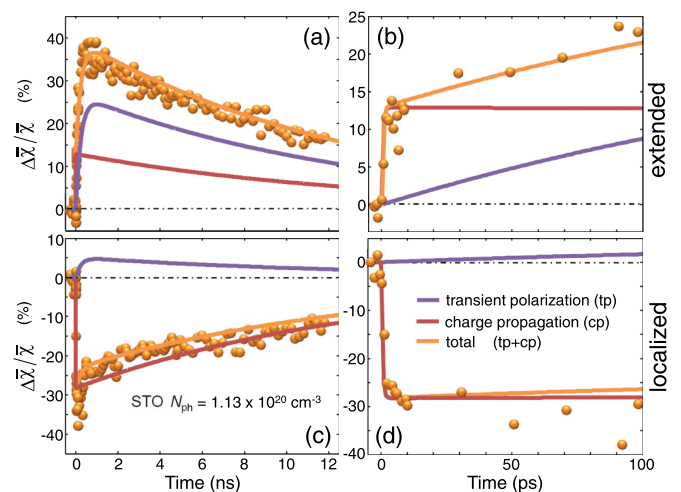


FIG. 3. Time dependence of the relative change in the SHG signal in STO after an optical excitation generating a photocarrier density of  $N_{\text{ph}} = 1.13 \times 10^{20} \text{ cm}^{-3}$  (data points). The fits reproduce this measured change (orange line) and its respective contributions from the charge-propagation (red line) and transient-polarization (blue line) mechanisms. SHG susceptibilities  $\bar{\chi}$  probe (c) and (d) the local state at the interface and (a) and (b) the extended environment around it.

( $pp$ );  $s$  in,  $p$  out ( $sp$ ); and  $d$  in,  $s$  out ( $ds$ ) [20]. These polarization combinations provide information on the three independent nonvanishing  $\chi_{ijk}$  components:  $\chi_{zzz}$ ,  $\chi_{\text{ext}}$ , and  $\chi_{\text{loc}}$ . In particular, the last two relevant terms are obtained directly from the  $sp$  and  $ds$  signal, respectively, while the  $pp$  signal is used only for an experimental check.

The same apparatus with slight modifications is used for measuring the linear reflectivity changes induced by the pump. In this case the filter used to block the fundamental beam is removed, and the photomultiplier that detects the SHG signal is replaced with a photodiode.

## IV. RESULTS

### A. Pump-probe SHG measurements

Let us first discuss our main experimental results, i.e., our pump-probe SHG measurements. Then, in Sec. IV B, we discuss our photoinduced reflectivity measurements in order to support some of our theoretical assumptions.

Figure 2(a) and the zoomed-in view in Fig. 2(b) show the time-dependent change in  $\chi_{\text{ext}}$  in the LS2 and LS6 samples and STO at a pump laser intensity of  $1 \text{ mJ cm}^{-2}$  (excitation density  $N_{\text{ph}} = 5.65 \times 10^{20} \text{ cm}^{-3}$ ). The samples show an initial subpicosecond drop in the SHG signal, followed by a recovery on the 100-ps time scale and restoration of the initial state over nanoseconds. With increasing LAO coverage,  $\Delta\bar{\chi}_{\text{ext}}/\bar{\chi}_{\text{ext}}$  evolves from positive to negative values. In LS2 and STO the ratio  $\Delta\bar{\chi}_{\text{ext}}/\bar{\chi}_{\text{ext}}$  becomes positive, implying a transient enhancement of the polarity of these samples by the photoexcitation, whereas in LS6 the relation  $\Delta\bar{\chi}_{\text{ext}}/\bar{\chi}_{\text{ext}} < 0$  indicates a transient attenuation of the polarity. Strikingly, the SHG susceptibility changes may amount to as much as  $\pm 30\%$ .

In Sec. V we will discuss in detail these findings within the framework of a phenomenological model able to capture the main features of this complex dynamics.

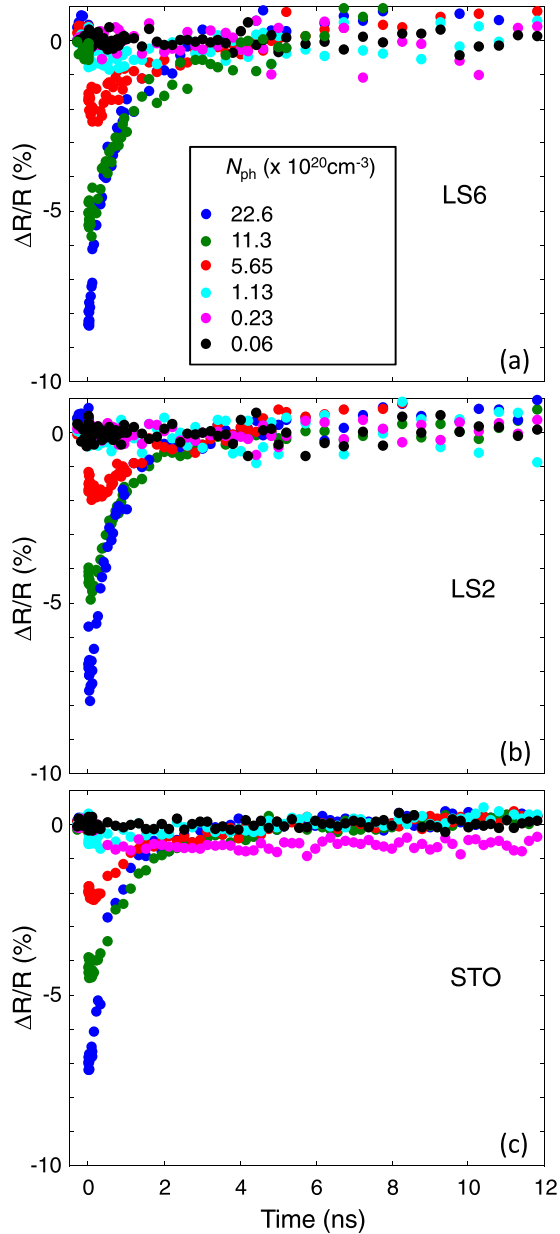


FIG. 4. Pump-induced changes in reflectivity as a function of the photocarrier density for the samples: (a) LS6, (b) LS2, and (c) STO.

### B. Photoinduced reflectivity changes

In Fig. 4 we report our time-resolved reflectivity measurements for different values of the pump fluence and for all the samples. The observed changes are due to transient variations of the refractive index. A change in the refractive index causes a variation of the Fresnel factors that enter in Eq. (1) and may lead to a consequent variation of the SHG signal. A variation of the reflectivity may also be caused by a transient redistribution of the electronic populations, also known as the state-filling effect. The latter may transiently change the  $\chi_{ijk}^{(2)}$  and  $\chi_{ijkl}^{(3)}$  tensors in Eq. (1), thus leading to a transient variation of the SHG signal as well. In the following, based on the data

reported in Fig. 4, we show that both these effects are negligible compared to the free-carrier effects that are accounted for by  $E_z^{\text{pol}}$  in Eq. (1).

For what concerns the Fresnel factors the refractive-index changes observed in the reflectivity measurements are small either as an absolute value or as relative variations among all the samples. Let us consider the SHG signal variations reported in Fig. 2. At this laser fluence the maximum reflectivity change is about 2% for all samples. By using the refractive indexes of STO [27] and the reflection Fresnel transformations [28] this leads to a variation of the refractive index of about 1.1%, approximately the same for both the fundamental and the second-harmonic wavelengths. Now, according to Eq. (1) with  $i = z$  and  $j = k = y$ , the Fresnel factors  $L_{zz}$  at  $2\omega$  and  $L_{yy}$  at  $\omega$  enter once and twice, respectively, in the  $\bar{\chi}_{\text{ext}}$  signal shown in Fig. 2. By inserting the variations of the refractive index in the corresponding Fresnel factors given by Eq. (A4) of Ref. [9] we find that  $L_{zz}$  and  $L_{yy}$  vary about 2% and 0.9%, respectively. This accounts for a total variation of 3.8%, which is approximately one order of magnitude less than the maximum variation observed in LS6 and STO and a factor of 6 less than in the case of LS2. If we repeat this calculation for the polarization combination data displayed in Fig. 3, we find that the total variation accounted for by the Fresnel factors is even less than 1%, while the maximum observed variation of the SHG signal is about 40%. Furthermore, the comparison among all the samples at a fixed fluence shows that the differences between the reflectivity spectra are not larger than 1%, at best. Again, by using the same calculation as before, this leads to a relative variation among the samples due to the Fresnel factors of less than 1%. This allows us to assume that the Fresnel factors vary too little to explain the absolute SHG signal variations or, in any case, they vary approximately in the same way for all the samples to explain the different dynamics observed among the samples at a fixed laser fluence. For all these reasons we neglect the Fresnel factors in our analysis.

Similarly, the comparison of the reflectivity spectra between conductive and insulating samples allows us to neglect any state-filling effect based on the following argument. The surface density of mobile charges at the LS6 interface is about  $10^{14} \text{ cm}^{-2}$  (we note that this number is a lower limit since it does not include the injected charges that become localized) [12]. In order to compare this number with the photocarrier density induced by our pump we should know the space extension of the electronic gas at the interface. On the value of the latter there is not a unanimous consensus. However, we may safely assume that, at room temperature, it is confined in a region of the order of 1 nm with a more extended tail of localized charges [29]. The latter number gives a mobile carrier density of about  $10^{20}$ – $10^{21} \text{ cm}^{-3}$ , which is comparable to the photocarrier density photoinduced in STO. This shows that the LS6 sample is already strongly populated, even in the absence of the pump. However, the reflectivity changes that we measure in the STO and LS6 samples are approximately the same. This excludes possible state-filling effects at the laser fluences used in our experiments. For these reasons we assume that  $\chi_{ijk}^{(2)}$  and  $\chi_{ijkl}^{(3)}$  are constant in time.

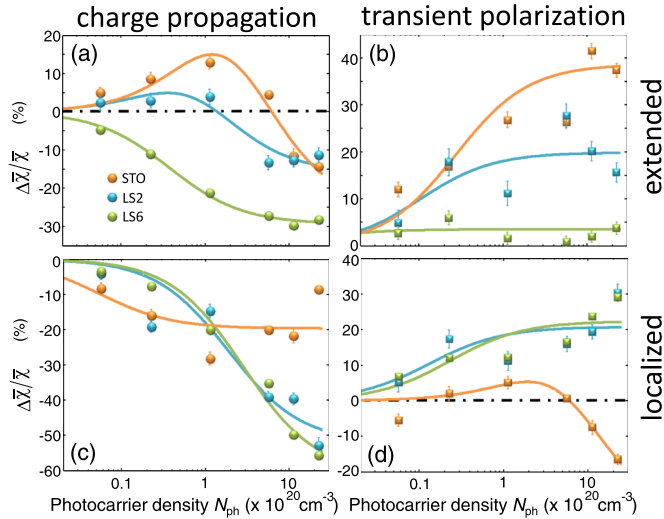


FIG. 5. Dependence of the relative change in the SHG susceptibility of the charge-propagation and transient-polarization contributions as defined in Eq. (3) on the density of the optical excitation  $N_{ph}$ . Symbols represent fits of Eq. (3) to measured data as in Fig. 3. The amplitudes have been normalized to the corresponding value of  $\bar{\chi}$  at time  $t < 0$ . Solid lines are fits (see text). Here and in Fig. 6 error bars indicate statistical errors at 68.3% of the confidence level obtained through a  $\chi^2$  test as described in Ref. [30]. The error bars are missing when their extension is not larger than symbol size.

## V. DISCUSSION

Before proceeding with the discussion, we need to identify the different types of contributions constituting the dynamics expressed in Fig. 2. We will focus this discussion on the simplest system, bare STO as depicted in Fig. 3, from which we will move on to further investigation of the LAO-covered samples in Figs. 5 and 6. First of all, we can exclude that photoinduced transfer of the STO from the quantum-paraelectric to a bulk ferroelectric state causes the transient SHG increase. On the one hand, laser illumination is known to suppress rather than promote ferroelectricity [31]. On the other hand, the isotropy of the bulk would support multidomain formation and thus cancellation of the net SHG signal. Instead, analysis of the STO dynamics in Fig. 3 reveals a simple model explaining our SHG data in a consistent way. Its mechanisms are pictorially outlined in Fig. 7.

(i) For *process 1* we assume that the pump beam creates an electron-hole plasma that perturbs the interface polarity of the ground state. The plasma gives rise to two competing mechanisms, both well established in semiconductors. The *first mechanism* is given by the drift of the photocarriers in the presence of a preexisting equilibrium electric field, here the interfacial field  $E_z^{pol}$ , in order to screen it [33,34]. We will refer to this as “screening drift” [Fig. 7(b)]. The *second mechanism* originates from the different mobilities of the photoexcited holes and electrons. The presence of the interface makes the diffusion anisotropic, thus inducing a net shift of the electron cloud with respect to the hole cloud. This gives rise to a local electric field at the interface [Fig. 7(c)]. In semiconductors this is known as the “photo-Dember effect” [35]. Henceforth, the parameters referring to electron-hole plasma generation and

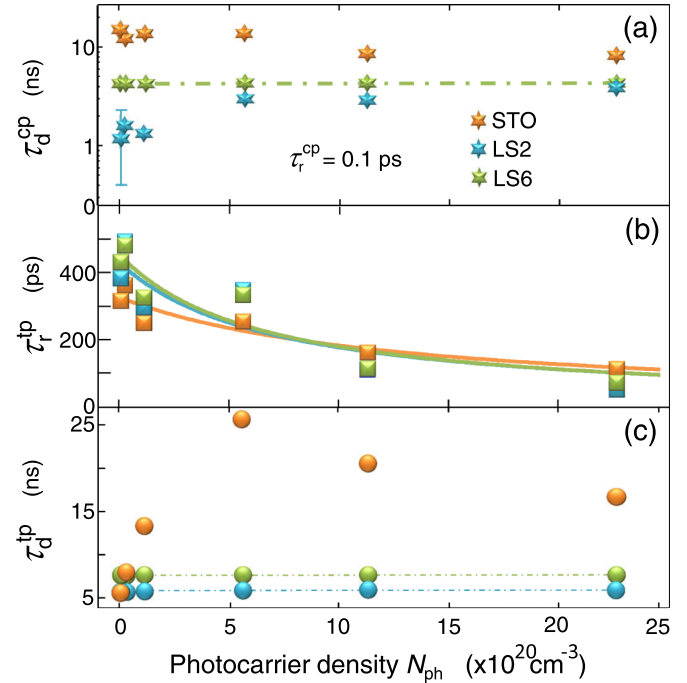


FIG. 6. Dependence of the relaxation constants defined in Eq. (3) on the density of the optical excitation in the three types of samples. Solid lines are fits (see text). Dot-dashed lines indicate values of relaxation constants that did not reveal a dependence on the photocARRIER density and were therefore replaced by a single fitting parameter over all the photocARRIER density range.

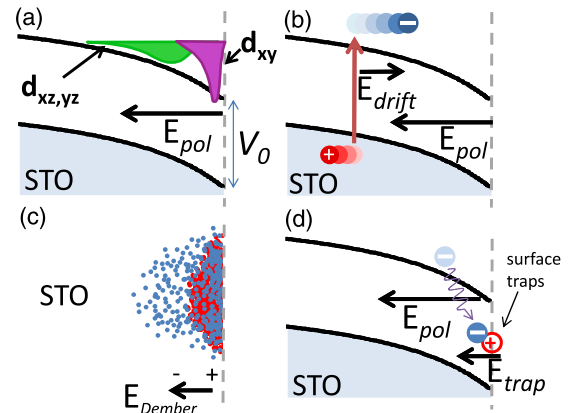


FIG. 7. Nonequilibrium charge dynamics near the LAO/STO and air/STO interfaces. (a) Band bending and different extension of the charge concentration associated with the  $d_{xy}$ -like and  $d_{xz,yz}$ -like subbands of STO at the interface (as adapted from Refs. [18,23]). We notice that the medium beyond the dashed line may be either air, like in bare STO, or a LAO overlayer. (b) Screening drift as the first process contributing to the charge-propagation mechanism. (c) Photo-Dember effect as the second process contributing to the charge-propagation mechanism (as adapted from Ref. [32]). (d) Interfacial charge trapping as the process contributing to the transient-polarization mechanism. Note the positive charge of the trapping center that induces an electric field that adds in phase to the existing quantum-well field, thus enhancing the interfacial polarity.

the two aforementioned *charge-propagation* mechanisms will be labeled cp.

(ii) For *process 2* we assume that the photogenerated carriers build up a transient polarization once they have reached the interface [Fig. 7(d)]. Mechanisms that may contribute to this polarization are interfacial charge trapping, polaron formation, etc. Henceforth, the parameters referring to the *transient-polarization* mechanism will be labeled tp.

By combining cp and tp contributions and assuming an exponential behavior for their rise (r) and decay (d), the temporal dynamic of  $\Delta\bar{\chi}_{\text{loc/ext}}$  is given by the equation

$$\begin{aligned} \Delta\bar{\chi}_{\text{loc/ext}} = & \Delta\bar{\chi}_{\text{loc/ext}}^{\text{cp}} \left(1 - e^{-t/\tau_r^{\text{cp}}}\right) e^{-t/\tau_d^{\text{cp}}} \\ & + \Delta\bar{\chi}_{\text{loc/ext}}^{\text{tp}} \left(1 - e^{-t/\tau_r^{\text{tp}}}\right) e^{-t/\tau_d^{\text{tp}}}. \end{aligned} \quad (3)$$

Here,  $\tau_{r,d}^{\text{cp,tp}}$  and  $\Delta\bar{\chi}_{\text{loc/ext}}^{\text{cp,tp}}$  denote the four time constants and the four SHG coupling coefficients, respectively.

Equation (3) yields a total of eight parameters for describing the SHG data of each type of sample (LS2, LS6, STO). Only a subset of these parameters needs to be fitted, however, to describe the photocarrier dynamics. For example,  $\tau_r^{\text{cp}}$  is resolution limited and thus fixed at 0.1 ps. Furthermore, different SHG susceptibilities for the same type of process obey the same time constants [e.g.,  $\tau_d^{\text{tp}}(\Delta\bar{\chi}_{\text{ext}}) = \tau_d^{\text{tp}}(\Delta\bar{\chi}_{\text{loc}})$ ]. We remark again that extended and localized states differ only for a few atomic layers; that is, both must be considered interfacial states. This makes barely detectable slight temporal differences between them. With these assumptions we obtain an excellent agreement between data and fit in Fig. 3.

Henceforth, this fit procedure allows us to disentangle charge propagation and transient polarization based on their different dynamics. We therefore resume data analysis on the LAO-covered samples. We varied the photoinduced carrier density  $N_{\text{ph}}$ , repeating the aforementioned fit procedure in each case. When  $\tau$  did not display a clear dependence on  $N_{\text{ph}}$ , we replaced it by a single value for all fits by a combined (global) fitting procedure. The resulting dependence of the SHG coupling coefficients and the time constants for the three types of samples are shown in Figs. 5 and 6 as a function of  $N_{\text{ph}}$ . In the following, we will discuss how the competition of the aforementioned photoinduced processes can explain the rich dynamics displayed in Figs. 5 and 6.

The amplitudes of the charge-propagation and transient-polarization processes as defined in Eq. (3) are plotted in Fig. 5 as a function of photocarrier density  $N_{\text{ph}}$ . The solid lines are fits obtained using the following function of the photocarrier density  $N_{\text{ph}}$ :

$$\Delta\bar{\chi}/\bar{\chi} \propto N_{\text{ph}} / (1 + N_{\text{ph}}/N_{\text{ph}}^{\text{sat}}), \quad (4)$$

where  $N_{\text{ph}}^{\text{sat}}$  is a fit parameter describing saturation effects, whose specific values are reported in Table I. A superposition of two of these functions with opposite signs is needed to take into account the zero-crossing behavior as a function of  $N_{\text{ph}}$  for some amplitudes [LS2 in Fig. 5(a) and STO in Figs. 5(a) and 5(d)]. This zero-crossing behavior is due to the competition between the screening-drift and photo-Dember mechanisms.

In fact, charge propagation is the result of screening drift, which enters the polarity balance with a negative sign ( $E_z^{\text{pol}}$  is screened), and the photo-Dember effect, which enters the

TABLE I. Values of  $N_{\text{ph}}^{\text{sat}}$  obtained through the fitting procedure explained in the text. Subscripts 1 and 2 correspond to the two fitting functions with opposite signs needed for taking into account the zero-crossing behavior as a function of  $N_{\text{ph}}$  for some amplitudes [LS2 in Fig. 5(a) and STO in Figs. 5(a) and 5(d)].

Sample	Extended ( $10^{20}\text{cm}^{-3}$ )				Localized ( $10^{20}\text{cm}^{-3}$ )			
	cp term		tp term		cp term		tp term	
	$N_{1\text{ph}}^{\text{sat}}$	$N_{2\text{ph}}^{\text{sat}}$	$N_{1\text{ph}}^{\text{sat}}$	$N_{2\text{ph}}^{\text{sat}}$	$N_{1\text{ph}}^{\text{sat}}$	$N_{2\text{ph}}^{\text{sat}}$	$N_{1\text{ph}}^{\text{sat}}$	$N_{2\text{ph}}^{\text{sat}}$
LS6	0.38		0.01		2.81		0.23	
LS2	0.73	0.76	0.10		1.89		0.13	
STO	1.94	2.03	0.27		0.05		5.26	5.31

polarity balance with a positive sign for electrons more mobile than holes. In the STO and LS2 systems, the electronic reconstruction with charge injection and interface conductance does not occur. Hence,  $E_z^{\text{pol}}$  is small or null, and the photo-Dember-like diffusion prevails over the screening drift: net polarity increases. When the electronic interface reconstruction occurs, either inherently in the LS6 sample or as a photoinduced effect with increasing photocarrier density,  $E_z^{\text{pol}}$  is large, and the screening drift prevails: net polarity decreases. The interplay of the two contributions explains the behavior yielded by the  $d_{xz,yz}$ -like subbands probed by  $\bar{\chi}_{\text{ext}}$  in Fig. 5(a). In contrast, the  $d_{xy}$ -like subband, probed by  $\bar{\chi}_{\text{loc}}$  in Fig. 5(c), shows only the decrease associated with the screening drift. Note that the photo-Dember effect describes an anisotropy in the charge propagation length that will become obvious only when an extended volume ( $\sim \bar{\chi}_{\text{ext}}$ ) is considered. In contrast, screening occurs all over the illuminated region and can therefore be perceived both when probing an extended region ( $\sim \bar{\chi}_{\text{ext}}$ ) and when probing a region atomically confined close to the interface ( $\sim \bar{\chi}_{\text{loc}}$ ).

As mentioned, the transient polarization builds up at the interface and increases the local electric field  $E_z^{\text{pol}}$ . Thus, the polarity change expressed by  $\Delta\bar{\chi}^{\text{tp}}(N_{\text{ph}})$  is positive in Figs. 5(b) and 5(d) and saturates with the photocarrier density. This saturation behavior indicates the participation in the process of a finite number of pinning centers in which photocarriers are trapped. We note that in LS6 the contribution of the extended state to the transient polarization is small but not null [Fig. 5(b)]. This might be a consequence of a major confinement of the 2DEG at the LS6 interface compared to LS2 and STO. Generally, STO surfaces are more defective, and hence, the trapping centers extend over a larger space region compared to LS2 and LS6. As a consequence, the extended states count more in STO and LS2 than in LS6. Interestingly, this hierarchy is reversed for the contribution from the localized states [see Fig. 5(d)], thus confirming our interpretation. A single exception to this understanding is the sign reversal of  $\Delta\bar{\chi}_{\text{loc}}^{\text{tp}}$  that occurs with increasing photocarrier density in STO. We speculate that this might be related to the specific influence of Fröhlich polarons, which are known to form on the STO surface but to be suppressed at the LAO/STO interface. [36]

Figure 6 scrutinizes the time scales of the charge-propagation and transient-polarization processes and reveals

two main tendencies: (i) The lifetimes of the charge-propagation contributions in the three types of samples are very different at low photocarrier density and quite similar at high photocarrier density. Thus, the difference between the insulating and the conducting samples reduces with increasing photocarrier density. A possible explanation for this could be that the conducting interface state that is inherently present in the LS6 sample is *photoinduced* in the STO and LS2 samples. Then the behavior of the LS2 sample would approach that of the LS6 sample with increasing  $N_{\text{ph}}$ , whereas the LS6 sample itself, in which the conducting interface state is already present at  $N_{\text{ph}} = 0$ , would reveal minor  $N_{\text{ph}}$  dependence. This is exactly what we observe in Fig. 6, and even though more evidence may be desirable, it strongly supports the scenario of a photoinduced conducting interface state.

(ii) The buildup time for the transient-polarization contributions in all types of samples ranges from tens to hundreds of picoseconds and decreases by an order of magnitude when the photocarrier density is increased by a factor 400 and reaches a common value for all the samples. As explained better in the following, the latter finding is a direct consequence of Eq. (5). Interestingly, the values of  $\tau_r^{\text{tp}}$  at low and intermediate values of  $N_{\text{ph}}$  are of the same order of magnitude of the time driving, at those laser fluences, the polaron formation as found in Ref. [8]. This time is also the same order of magnitude as that observed for the formation of a polaronic state in bulk STO [37]. Moreover, at the lowest fluences, we find that this time is slowed down in LS6, i.e., in the presence of the LAO overlayer. Although we observe a smaller slowing-down effect on  $\tau_r^{\text{tp}}$ , this observation is consistent with that reported by Yamada *et al.* [8], who attribute this effect to the presence of a strong interfacial electric field at the conductive LAO/STO interfaces, as LS6 is.

All these observations and analogies indicate polarons are good candidates for explaining the transition polarization state we observe. However, the lattice deformation accompanying the polaronic state must break the inversion symmetry to be visible in SHG. This might occur close to the interface where the photogenerated polarons may be trapped by defects and become polar in the presence of the interface. As already underlined, this trapping mechanism is proved by the saturation behavior of  $\Delta\bar{\chi}^{\text{tp}}$  as a function of  $N_{\text{ph}}$ . It is further confirmed by the nonlinear behavior of  $\tau_r^{\text{tp}}$  as a function of  $N_{\text{ph}}$ . We fitted the dependence of  $\tau_r^{\text{tp}}$  on  $N_{\text{ph}}$  with the relation

$$\tau_r^{\text{tp}} = \frac{\tau_{r0}^{\text{tp}}}{1 + AN_{\text{ph}}} + \tau_{\text{tr}}, \quad (5)$$

where the time at null laser fluence  $\tau_{r0}^{\text{tp}}$  is probably fixed by the drifting time needed for the polarons to reach the interface, the term linear in  $N_{\text{ph}}$  describes the enhancement of the probability per unit time of filling a pinning center, and  $\tau_{\text{tr}}$  is related to the intrinsic polaron formation time and/or to the intrinsic trapping cross section. Because  $\tau_{\text{tr}}$  is an intrinsic time of a process originating in STO, it is not surprising that  $\tau_r^{\text{tp}}$  becomes the same for all the samples at the highest fluences, as shown in Fig. 6(b). The decrease in  $\tau_r^{\text{tp}}$  with  $N_{\text{ph}}$  correlates well with the observed saturation behavior of  $\Delta\bar{\chi}^{\text{tp}}$  as a function of  $N_{\text{ph}}$  since a decrease in  $\tau_r^{\text{tp}}$  accelerates filling of the pinning centers.

TABLE II. Values of  $A$  and  $\tau_{r0}^{\text{tp}}$  obtained through the fitting procedure explained in the text.

Sample	$A$ ( $10^{-20} \text{ cm}^3$ )	$\tau_{r0}^{\text{tp}}$ (ps)
LS6	0.15–0.21	407–453
LS2	0.14–0.20	383–430
STO	0.08–0.12	280–327

The fitting parameters entering Eq. (5) are, in principle,  $A$ ,  $\tau_{r0}^{\text{tp}}$ , and  $\tau_{\text{tr}}$ . Given the limited dynamic range of our measurements and the large scattering of our data,  $\tau_{\text{tr}}$  cannot be determined precisely. Therefore, we keep it fixed in our fits. We get consistently good fits by varying  $\tau_{\text{tr}}$  in the range of 50 to 0 ps. We note that this time scale is compatible with that reported in Ref. [8]. The corresponding value intervals obtained for  $A$  and  $\tau_{r0}^{\text{tp}}$  are reported in Table II. We note that  $\tau_{r0}^{\text{tp}}$  increases by going from bare STO to LS6.

The polaronic mechanism is further confirmed by the following argument. In conducting LAO/STO, the free-carrier mobility at room temperature is about  $5 \text{ cm}^2 \text{ V}^{-1} \text{ s}^{-1}$ , which is in stark contrast to our measured drift time on the order of 100 ps [38]. The drift mobility of polarons in STO, however, was found to be  $0.04 \text{ cm}^2 \text{ V}^{-1} \text{ s}^{-1}$ , i.e., two orders of magnitude slower [39]. Assuming an electric field generated by a quantum well of about  $40 \text{ mV nm}^{-1}$  thus yields a polaron drift velocity of about  $16 \times 10^{10} \text{ nm s}^{-1}$  [40]. With a pump-laser penetration depth of 26 nm we find a transit time of the polarons toward the interface of about 160 ps, fully compatible with our measured values. We note that 160 ps is a lower limit since the electric field becomes weaker and weaker far from the interface where the polaron motion has a mainly diffusive character.

Finally, we observe that, with the notable exception of the localized state in STO at the highest fluences [Fig. 5(d)], the transient polarization state always increases the existent interfacial polarity. This means that the electric-field buildup by the transient polarization state adds in phase to that of the quantum well. Probably, this is a consequence of the presence at the interface of oxygen vacancies that are positively charged, as schematically shown in Fig. 7(d).

## VI. CONCLUSIONS

In conclusion, we have shown that photodoping can transiently change the polarity of the LAO/STO interface by more than 50% within a few picoseconds. The polarity change is the consequence of competing charge-carrier-dynamical processes, namely, charge propagation in the form of screening drift and the photo-Dember effect, on the one hand, and interfacial transient polarization buildup, on the other hand. The latter is probably due to the formation of polarons that drift toward the interface, where they are eventually trapped.

Finally, we note that our LS6 interface is characterized by the coexistence of both a polar order and a metallic state. Analogous systems, also known as *polar metals*, are deeply investigated nowadays for the possibility of obtaining “new multifunctional materials with unusual coexisting properties, such as anisotropic thermoelectric responses and magnetoelectric multiferroics, paving the way

for a new generation of devices with the ability to perform simultaneous electrical, magnetic and optical functions” [41]. In this respect our approach might be extended to this new generation of materials and related devices in order to control their properties on an ultrafast time scale with an enormous potential for applications.

## ACKNOWLEDGMENTS

We acknowledge funding from the European Union (FP7-PEOPLE-2012-CIG, Grant Agreement No. PCIG12-GA-2012-326499-FOXIDUET) and the Deutsche Forschungsgemeinschaft (SFB 608 and TRR 80).

- 
- [1] H. Y. Hwang, Y. Iwasa, M. Kawasaki, B. Keimer, N. Nagaosa, and Y. Tokura, Emergent phenomena at oxide interfaces, *Nat. Mater.* **11**, 103 (2012).
- [2] A. Ohtomo and H. Y. Hwang, A high-mobility electron gas at the  $\text{LaAlO}_3/\text{SrTiO}_3$  heterointerface, *Nature (London)* **427**, 423 (2004).
- [3] S. Thiel, G. Hammerl, A. Schmehl, C. Schneider, and J. Mannhart, Tunable quasi-two-dimensional electron gases in oxide heterostructures, *Science* **313**, 1942 (2006).
- [4] L. Li, C. Richter, J. Mannhart, and R. C. Ashoori, Coexistence of magnetic order and two-dimensional superconductivity at  $\text{LaAlO}_3/\text{SrTiO}_3$  interfaces, *Nat. Phys.* **7**, 762 (2011).
- [5] M. Huijben, G. Rijnders, D. H. A. Blank, S. Bals, S. Van Aert, J. Verbeeck, G. Van Tendeloo, A. Brinkman, and H. Hilgenkamp, Electronically coupled complementary interfaces between perovskite band insulators, *Nat. Mater.* **5**, 556 (2006).
- [6] P. Irvin, Y. J. Ma, D. F. Bogorin, C. Cen, C. W. Bark, C. M. Folkman, C. B. Eom, and J. Levy, Rewritable nanoscale oxide photodetector, *Nat. Photonics* **4**, 849 (2010).
- [7] A. Tebano, E. Fabbri, D. Pergolesi, G. Balestrino, and E. Traversa, Room-temperature giant persistent photoconductivity in  $\text{SrTiO}_3/\text{LaAlO}_3$  heterostructures, *ACS Nano* **6**, 1278 (2012).
- [8] Y. Yamada, H. K. Sato, Y. Hikita, H. Y. Hwang, and Y. Kanemitsu, Measurement of the Femtosecond Optical Absorption of  $\text{LaAlO}_3/\text{SrTiO}_3$  Heterostructures: Evidence for an Extremely Slow Electron Relaxation at the Interface, *Phys. Rev. Lett.* **111**, 047403 (2013).
- [9] A. Rubano, M. Fiebig, D. Paparo, A. Marino, D. Maccariello, U. S. di Uccio, F. M. Granozio, L. Marrucci, C. Richter, S. Pätel, and J. Mannhart, Spectral and spatial distribution of polarization at the  $\text{LaAlO}_3/\text{SrTiO}_3$  interface, *Phys. Rev. B* **83**, 155405 (2011).
- [10] Y. Tokura, Multiferroics—Toward strong coupling between magnetization and polarization in a solid, *J. Magn. Magn. Mater.* **310**, 1145 (2007).
- [11] M. Trassin, G. De Luca, S. Manz, and M. Fiebig, Probing Ferroelectric Domain Engineering in  $\text{BiFeO}_3$  Thin Films by Second Harmonic Generation, *Adv. Mater.* **27**, 4871 (2015).
- [12] A. Savoia, D. Paparo, P. Perna, Z. Ristic, M. Salluzzo, F. M. Granozio, U. S. di Uccio, C. Richter, S. Thiel, J. Mannhart, and L. Marrucci, Polar catastrophe and electronic reconstructions at the  $\text{LaAlO}_3/\text{SrTiO}_3$  interface: Evidence from optical second harmonic generation, *Phys. Rev. B* **80**, 075110 (2009).
- [13] N. Ogawa, K. Miyano, M. Hosoda, T. Higuchi, C. Bell, Y. Hikita, and H. Y. Hwang, Enhanced lattice polarization in  $\text{SrTiO}_3/\text{LaAlO}_3$  superlattices measured using optical second-harmonic generation, *Phys. Rev. B* **80**, 081106(R) (2009).
- [14] Y. R. Shen, Surfaces Probed by Nonlinear Optics, *Surf. Sci.* **299/300**, 551 (1994).
- [15] T. Günter, A. Rubano, D. Paparo, M. Lilienblum, L. Marrucci, F. Miletto Granozio, U. Scotti di Uccio, R. Jany, C. Richter, J. Mannhart, and M. Fiebig, Spatial inhomogeneities at the  $\text{LaAlO}_3/\text{SrTiO}_3$  interface: Evidence from second harmonic generation, *Phys. Rev. B* **86**, 235418 (2012).
- [16] A. Rubano, T. Günter, T. Fink, D. Paparo, L. Marrucci, C. Cancellieri, S. Gariglio, J.-M. Triscone, and M. Fiebig, Influence of atomic termination on the  $\text{LaAlO}_3/\text{SrTiO}_3$  interfacial polar rearrangement, *Phys. Rev. B* **88**, 035405 (2013).
- [17] A. Rubano, C. Aruta, U. S. di Uccio, F. M. Granozio, L. Marrucci, T. Günter, T. Fink, M. Fiebig, and D. Paparo, Electronic states at polar/nonpolar interfaces grown on  $\text{SrTiO}_3$  studied by optical second harmonic generation, *Phys. Rev. B* **88**, 245434 (2013).
- [18] G. De Luca, A. Rubano, E. di Gennaro, A. Khare, F. M. Granozio, U. S. di Uccio, L. Marrucci, and D. Paparo, Potential-well depth at amorphous- $\text{LaAlO}_3$ /crystalline- $\text{SrTiO}_3$  interfaces measured by optical second harmonic generation, *Appl. Phys. Lett.* **104**, 261603 (2014).
- [19] A. Rubano, G. De Luca, J. Schubert, Z. Wang, S. Zhu, D. G. Schlom, L. Marrucci, and D. Paparo, Polar asymmetry of  $\text{La}_{(1-\delta)}\text{Al}_{(1+\delta)}\text{O}_3/\text{SrTiO}_3$  heterostructures probed by optical second harmonic generation, *Appl. Phys. Lett.* **107**, 101603 (2015).
- [20] D. Paparo, A. Rubano, and L. Marrucci, Optical second-harmonic generation selection rules and resonances in buried oxide interfaces: The case of  $\text{LaAlO}_3/\text{SrTiO}_3$ , *J. Opt. Soc. Am. B* **30**, 2452 (2013).
- [21] A. J. Sabbah and D. M. Riffe, Femtosecond pump-probe reflectivity study of silicon carrier dynamics, *Phys. Rev. B* **66**, 165217 (2002).
- [22] Z. S. Popović, S. Satpathy, and R. M. Martin, Origin of the Two-Dimensional Electron Gas Carrier Density at the  $\text{LaAlO}_3$  on  $\text{SrTiO}_3$  Interface, *Phys. Rev. Lett.* **101**, 256801 (2008).
- [23] P. Delugas, A. Filippetti, V. Fiorentini, D. I. Bilc, D. Fontaine, and P. Ghosez, Spontaneous 2-Dimensional Carrier Confinement at the  $n$ -Type  $\text{SrTiO}_3/\text{LaAlO}_3$  Interface, *Phys. Rev. Lett.* **106**, 166807 (2011).
- [24] N. C. Plumb, M. Salluzzo, E. Razzoli, M. Månsson, M. Falub, J. Krempasky, C. E. Matt, J. Chang, M. Schulte, J. Braun, H. Ebert, J. Minár, B. Delley, K.-J. Zhou, T. Schmitt, M. Shi, J. Mesot, L. Patthey, and M. Radović, Mixed Dimensionality of Confined Conducting Electrons in the Surface Region of  $\text{SrTiO}_3$ , *Phys. Rev. Lett.* **113**, 086801 (2014).
- [25] D. Goldschmidt and H. L. Tuller, Fundamental absorption-edge of  $\text{SrTiO}_3$  at high-temperatures, *Phys. Rev. B* **35**, 4360 (1987).
- [26] M. I. Cohen and R. F. Blunt, Optical properties of  $\text{SrTiO}_3$  in the region of the absorption edge, *Phys. Rev.* **168**, 929 (1968).
- [27] Refractive index database, <https://refractiveindex.info/?shelf=main&book=SrTiO3&page=Dodge>.
- [28] Fresnel equations, [https://en.wikipedia.org/wiki/Fresnel\\_equations](https://en.wikipedia.org/wiki/Fresnel_equations).

- [29] C. Cantoni, J. Gazquez, F. M. Granozio, M. P. Oxley, M. Varela, A. R. Lupini, S. J. Pennycook, C. Aruta, U. Scotti di Uccio, P. Perna, and D. Maccariello, Electron transfer and ionic displacements at the origin of the 2d electron gas at the LAO/STO interface: Direct measurements with atomic-column spatial resolution, *Adv. Mater.* **24**, 3952 (2012).
- [30] W. H. Press, B. P. Flannery, S. A. Teukolsky, and W. T. Vetterling, *Numerical Recipes in Pascal* (Cambridge University Press, New York, 1989).
- [31] Y. Yamada and K. Tanaka, Photo-induced suppression of ferroelectric transition in oxygen-isotope-exchanged SrTiO<sub>3</sub>, *J. Lumin.* **112**, 259 (2005).
- [32] Photo-Dember effect, [https://en.wikipedia.org/wiki/Photo%E2%80%93Dember\\_effect](https://en.wikipedia.org/wiki/Photo%E2%80%93Dember_effect).
- [33] T. Dekorsy, T. Pfeifer, W. Kütt, and H. Kurz, Subpicosecond carriers transport in GaAs surface-space-charge fields, *Phys. Rev. B* **47**, 3842 (1993).
- [34] Y. M. Chang, Y. L. Hong, and S. Gwo, Direct probe of the built-in electric field of Mg-doped a-plane wurtzite InN surfaces with time-resolved electric-field-induced second harmonic generation, *Appl. Phys. Lett.* **93**, 131106 (2008).
- [35] H. Dember, Über eine photoelektronische Kraft in Kupferoxydul-Kristallen (Photoelectric E. M. F. in Cuprous-Oxide Crystals), *Phys. Z.* **32**, 554 (1931).
- [36] C. Cancellieri, A. S. Mishchenko, U. Aschauer, A. Filippetti, C. Faber, O. S. Barisic, V. A. Rogalev, T. Schmitt, N. Nagaosa, and V. N. Strocov, Polaronic metal state at the LaAlO<sub>3</sub>/SrTiO<sub>3</sub> interface, *Nat. Commun.* **7**, 10386 (2016).
- [37] T. Kohmoto, D. Ikeda, X. Liang, and T. Moriyasu, Direct observation of the spatial and temporal dynamics of polaron diffusion in SrTiO<sub>3</sub>, *Phys. Rev. B* **87**, 214301 (2013).
- [38] W. Siemons, G. Koster, H. Yamamoto, W. A. Harrison, G. Lucovsky, T. H. Geballe, D. H. A. Blank, and M. R. Beasley, Origin of Charge Density at LaAlO<sub>3</sub> on SrTiO<sub>3</sub> Heterointerfaces: Possibility of Intrinsic Doping, *Phys. Rev. Lett.* **98**, 196802 (2007).
- [39] D. Kéroack, Y. Lépine, and J. L. Brebner, Drift mobility measurements of small-polaron transport in SrTiO<sub>3</sub>, *J. Phys. C* **17**, 833 (1984).
- [40] P. W. Lee, V. N. Singh, G. Y. Guo, H.-J. Liu, J.-C. Lin, Y.-H. Chu, C. H. Chen, and M.-W. Chu, Hidden lattice instabilities as origin of the conductive interface between insulating LaAlO<sub>3</sub> and SrTiO<sub>3</sub>, *Nat. Commun.* **7**, 12773 (2016).
- [41] T. H. Kim, D. Puggioni, Y. Yuan, L. Xie, H. Zhou, N. Campbell, P. J. Ryan, Y. Choi, J.-W. Kim, J. R. Patzner, S. Ryu, J. P. Podkaminer, J. Irwin, Y. Ma, C. J. Fennie, M. S. Rzchowski, X. Q. Pan, V. Gopalan, J. M. Rondinelli, and C. B. Eom, Polar metals by geometric design, *Nature (London)* **533**, 68 (2016).